Korean J. Chem. Eng., 33(6), 1823-1830 (2016)
DOI: 10.1007/s11814-016-0026-5

pISSN: 0256-1115
eISSN: 1975-7220

Catalytic oxidation and capture of elemental mercury from simulated flue gas using Mn-doped titanium dioxide

Jingtao Zhi*, Xianqun Yu*, Jingjing Bao, Xiaoxiang Jiang**, and Hongmin Yang***,†**

*School of Energy & Mechanical Engineering, Nanjing Normal University, Nanjing 210042, P. R. China
**Jiangsu Provincial Key Laboratory of Materials Cycling and Pollution Control, Nanjing 210042, P. R. China
***Engineering Laboratory for Energy System Process Conversion & Emission Control Technology of Jiangsu Province, Nanjing 210042, P. R. China

(*Received 9 October 2015 • accepted 25 January 2016*)

Abstract−Titanium dioxide (TiO_2) and Mn-doped TiO_2 (Mn(x)-TiO_2) were synthesized in a sol-gel method and characterized by BET surface area analysis, X-ray diffraction (XRD) and X-ray photoelectron spectroscopy (XPS). Gas-phase elemental mercury (Hg^0) oxidation and capture by the Mn-doped TiO_2 catalyst was studied in the simulated flue gas in a fixed-bed reactor. The investigation of the influence of Mn loading, flue gas components (SO_2, NO, O_2, and H_2O) showed that the Hg^0 capture capability of Mn(x)-TiO_2 was much higher than that of pure TiO_2. The addition of Mn inhibits the grain growth of TiO_2 and improves the porous structure parameters of Mn(x)-TiO_2. Excellent Hg^0 oxidation performance was observed with the catalyst with 10% of Mn loading ratio and 97% of Hg^0 oxidation was achieved under the test condition (120 °C, N_2/6%O_2). The presence of O_2 and NO had positive effect on the Hg^0 removal efficiency, while mercury capture capacity was reduced in the presence of SO_2 and H_2O. XPS spectra results reveal that the mercury is mainly present in its oxidized form (HgO) in the spent catalyst and Mn^{4+} doped on the surface of TiO_2 is partially converted into Mn^{3+} which indicates Mn and the lattice oxygen are involved in Hg^0 oxidation reactions.

Keywords: Elemental Mercury, Mn-doped Titanium Dioxide, Catalytic Oxidation, Removal

INTRODUCTION

Mercury emissions have attracted increasing attention due to their adverse effects on human health and ecosystem [1]. Mercury emitted from coal-fired power plants accounts for the largest part of atmospheric mercury emission [2]. It is necessary to deal with the mercury pollution released from power plants. More than 20 U.S. states had proposed or adopted rules used to limit mercury emissions from coal-fired power plants by April 2010 [3]. The US Environmental Protection Agency (EPA) announced the Mercury and Air Toxics Standards (MATS) in December 2011, aiming to control emission of mercury and other toxic pollutants from power plants [4].

Mercury exists in flue gas as three forms: gaseous elemental mercury (Hg^0), oxidized mercury (Hg^{2+}), and particle-bound mercury (Hg^p) [5]. Among these, Hg^p can be collected by an electrostatic precipitator (ESP) and/or a baghouse. Hg^{2+} is water-soluble, and thus can be captured effectively by wet flue gas desulfurization (WFGD) equipment. However, because of high volatility, low solubility in water and poor reactivity with fly ash for Hg^0 [6], it is difficult to remove by conventional air pollution control devices (APCDs). It is likely to enter the global atmospheric cycle. Accordingly, removal of Hg^0 from flue gas has attracted much more attention.

Bench scale studies show that metal oxide SCR catalysts can oxidize Hg^0 to Hg^{2+}. The catalysts employed in the selective catalytic reduction (SCR) for nitric oxides have been proven to significantly increase oxidation of elemental mercury, which can be effectively captured by FGD downstream [7]. This co-benefit from SCR makes the cost of mercury control more economical than the ACI method. Unlike commercial SCR catalysts, low temperature SCR catalysts operate at 100-250 °C, making it possible to move the catalyst bed downstream of the particulate collector, where the temperature is normally below 150 °C. The catalysts based on the transition metal oxides have been developed and proven to be effective for nitric oxides and mercury removal in lower temperature SCR catalyst [9-12]. Since alumina supported manganese dioxide shows mercury capacity in the temperature range of 60-177 °C, it is possible that a low-temperature SCR catalyst (titania supported manganese oxide) can also serve as an elemental mercury oxidant and adsorbent [8].

The manganese oxides in catalysts were demonstrated to be the active ingredient in Hg^0 oxidation process. He et al. [10] used the MnOx/TiO_2 modified by the CeO_2 to capture the Hg^0 and NO, and found that 20 wt% MnOx/CeO_2-TiO_2 removed 9.4 mg Hg^0 g^{-1} and 358 mg NO g^{-1} at 175 °C. Yang et al. [11] prepared Mn-Fe catalyst by a coprecipitation method and found the catalyst was highly active for Hg^0 oxidation. Ji et al. [13] reported that manganese based catalysts also showed remarkable mercury capture capacity (17.4 mg/g) at 200 °C, which was much higher than that of activated carbon. The reaction mechanism for Hg^0 oxidation over manganese

†To whom correspondence should be addressed.
E-mail: yanghongmin@njnu.edu.cn

based catalysts was supposed to be the Mars-Maessen mechanism as follows [14].

$$Hg^0(g)+catalysts \rightarrow Hg^0(ad) \quad (1)$$

$$Hg^0(ad)+Mn_xO_y \rightarrow HgO+Mn_xO_{y-1} \quad (2)$$

The purpose of this work is to verify the catalytic oxidation and capture of elemental mercury on Mn-doped titanium dioxide at low temperature. This paper presents the results of a study on the potential of the Mn-doped TiO_2 catalyst synthesized with a sol-gel method for the capture of vapor phase elemental mercury. The dynamic mercury capture behavior of the catalyst in the simulated flue gas was tested in a lab-scale fixed-bed reactor. The effects of the manganese loading and the main components of flue gas, such as moisture, oxygen, sulfur dioxide, nitric oxide, on mercury removal efficiency were also investigated. Meanwhile, the essential analysis and characterization of catalysts were also conducted to reveal the possible mechanism of Hg^0 adsorption and conversion on the catalysts.

EXPERIMENTAL SECTION

1. Material and Preparation

Chemicals used in catalyst preparation were commercial products purchased from Nanjing Chemical Reagent Company and all of them were analytical grade. In typical synthesis of Mn(x)-TiO_2 with Mn content in the range of 1-15 mol% (Mn/(Mn+Ti); denoted as Mn(1)-TiO_2, Mn(3)-TiO_2, Mn(5)-TiO_2, Mn(10)-TiO_2 and Mn(15)-TiO_2) were prepared by a sol-gel method. 25 mL tetrabutyl titanate and 4 ml HNO_3 (6 mol/L) were dissolved in 75 mL anhydrous ethanol under vigorous stirring. After being stirred for 1 hour, a mixture of specific amounts of manganese nitrate and 25 mL anhydrous ethanol and 5 mL distilled water (the pH was adjusted to 2.0) was added dropwise to the solution. The resultant gel was dried at 100 °C overnight and calcined at 500 °C in air for 3 h. Then the prepared adsorption-catalytic oxidation adsorbents were ground to powder.

2. Material Characterization

The TiO_2 and Mn(x)-TiO_2 were characterized by different analytic techniques. The Brunauer-Emmett-Teller (BET) surface area and porous structure properties of the catalysts were determined using a Quantachrome Nova 1000e (U.S.A.). The crystal phase of Mn(x)-TiO_2 was characterized by X-ray diffraction (XRD). The XRD patterns were recorded on a D/max-2500/PC X-ray diffractometer with a Cu Kα radiation source over the range of 2θ from 5° to 85°. The scanning speed was 0.02°s^{-1}. The chemical compositions on the surface of the catalysts were studied by X-ray photoelectron spectra (Kratos Axis Ultra DLD spectrometer) with a monochromatic Al Kα X-ray source. All binding energies were corrected by setting the binding energy of the surface adventitious carbon (C 1s) at 284.8 eV.

3. Experimental Setup

The experimental apparatus, shown in Fig. 1, includes the generator of simulated flue gas, the fixed-bed catalytic reactor, the temperature-controlled furnace, and the online gas and mercury analyzer. The simulated flue gas was consisted of O_2, SO_2, H_2O, NO and balanced with N_2, which was provided by gas cylinders (Nanjing Gas Company, China). The flow rate of the gas stream was accurately controlled by the mass flow controller (MFC) (Beijing Metron Instrument Company, China). Nitrogen flow was divided into three branches. The first stream was mixed with SO_2, NO and O_2 to form the main gas flow. The second N_2 stream passed through the Hg^0 permeation tube (VICI Metronics, Inc., USA) placed inside a U-shaped glass tube to carry Hg^0. The U-shaped glass tube was immersed in a water bath with a constant temperature of (45± 1 °C). The third N_2 stream was used to introduce humid flow by passing through a heated water bath. The total flow rate of the simulated flue gas remained constant at 2.2 L·min^{-1}.

The reactor is a U-shaped quartz tube (with an inner diameter of 15 mm) located inside a temperature-controlled furnace. The

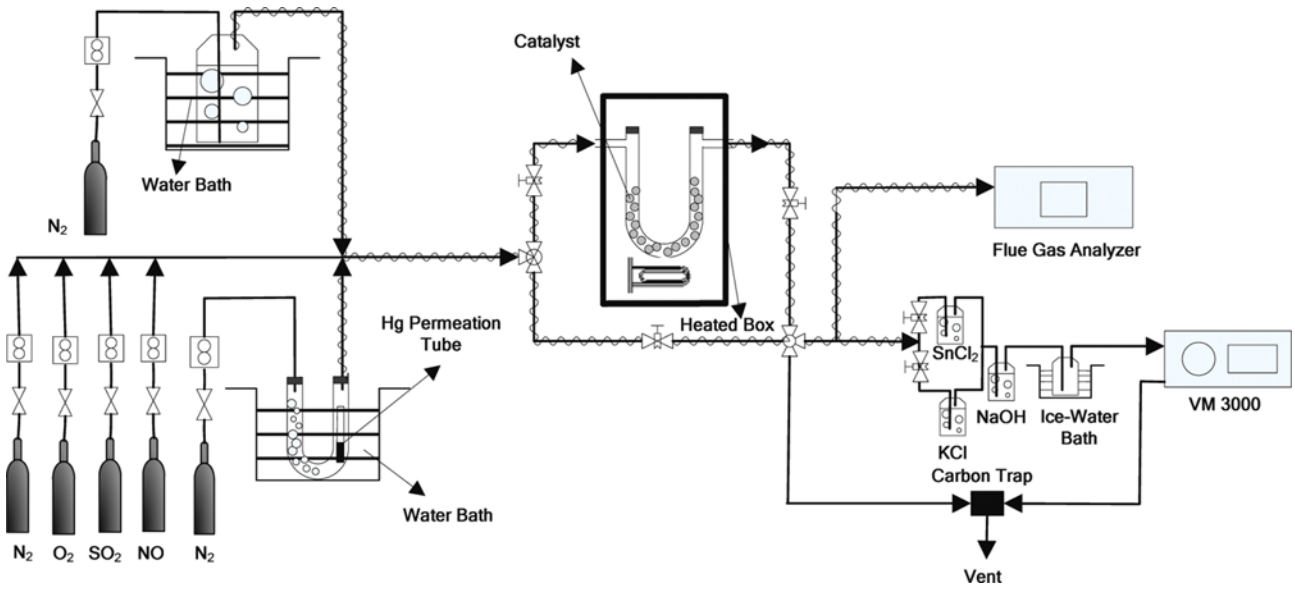

Fig. 1. Schematic diagram of experimental system.

reaction temperature was controlled at 120 °C. Quartz had been demonstrated to have good chemical resistance and inertness toward mercury. To avoid adsorption of mercury, all the connected pipelines were made of Teflon and heated to 120 °C by electrical heating tapes. The concentration of gas components was measured by ECOMJ2KN (RBR Company, German). The concentration of gaseous mercury was monitored by VM3000 mercury analyzer (Mercury Instrument Company, German) with a Hg speciation conversion system [15]. In the conversion system, the sample flow was divided into two streams in the conversion system. One stream passed through 10% $SnCl_2$ solution, which reduced the oxidized mercury to the elemental mercury, then the concentration of total mercury (Hg^T) was measured. The other stream passed through 10% KCl solution directly, which captured oxidized mercury (Hg^{2+}) and allowed Hg^0 to pass through only. Therefore, the concentration of oxidized mercury (Hg^{2+}) could be determined based on the difference of Hg^T and Hg^0 concentration. Prior to entering the VM3000 Hg^0 analyzer, the two streams went through the adsorption bottle containing 5% NaOH solution, and then the condenser to remove acid gases and water vapor. The total mercury adsorbed on the spent catalysts was determined using Leeman advanced mercury analyzer---Hydra C II (Teledyne Leeman Labs, USA).

4. Test Conditions

To better understand Hg^0 capture behavior over Mn-TiO_2 catalyst in the flue gas, Hg^0 capture experiments were carried out under N_2, N_2+O_2, N_2+SO_2, N_2+NO and N_2+O_2+SO_2+NO+H_2O complex atmospheres. The experimental conditions are listed in Table 1. Set 1 was aimed to investigate the role of Mn addition on the elemental mercury oxidation and capture. In sets 2, 3, 4 and 5, the effects of individual flue gas components (O_2, NO, SO_2, H_2O) and the complex flue gas on mercury oxidation and capture were studied, respectively.

The Hg^0 and Hg^T removal efficiency at a particular time (t_i) is defined as follows:

$$\eta^i_{Hg^0}(\%) = \frac{Hg^0_{in} - Hg^0_{out}}{Hg^0_{in}} \times 100\% \quad (3)$$

$$\eta^i_{Hg^T}(\%) = \frac{Hg^T_{in} - Hg^T_{out}}{Hg^T_{in}} \times 100\% \quad (4)$$

where Hg^0_{in} and Hg^0_{out} are the inlet and outlet concentration of elemental mercury (Hg^0), Hg^T_{in} and Hg^T_{out} are the inlet and outlet concentration of the total mercury, respectively.

The average Hg^0 and average Hg^T removal efficiency during the reaction period are defined as follows:

Table 2. Porous structure parameters of the catalysts

Samples	Specific surface area ($m^2 \cdot g^{-1}$)	Pore volume ($cm^3 \cdot g^{-1}$)	Average pore size (nm)
TiO_2	20.5	0.030	3.87
Mn(1)-TiO_2	26.2	0.039	3.87
Mn(3)-TiO_2	41.2	0.052	3.86
Mn(5)-TiO_2	80.2	0.133	5.44
Mn(10)-TiO_2	104.9	0.179	4.84
Mn(15)-TiO_2	102.6	0.163	4.79

$$E_{Hg^0}(\%) = \frac{\sum_{i=1}^{n} \eta^i_{Hg^0}}{n} \times 100\% \quad (5)$$

$$E_{Hg^T}(\%) = \frac{\sum_{i=1}^{n} \eta^i_{Hg^T}}{n} \times 100\% \quad (6)$$

RESULTS AND DISCUSSION

1. Catalyst Characterization

The porous structure parameters of the prepared catalysts are listed in Table 2. It is obvious that the Mn(10)-TiO_2 has the highest BET surface area (approximately 104.9 $m^2 \cdot g^{-1}$) and largest pore volume (approximately 0.179 $cm^3 \cdot g^{-1}$). Pure TiO_2 exhibited a low specific surface area of 20.5 m^2/g. The addition of Mn inhibited the grain growth of TiO_2 crystalline. After Mn^{4+} entered the TiO_2 lattice, some parts of Ti^{4+} would be substituted, which caused the lattice distortion. The pore size of the catalyst trended to increase, and then increased the specific surface area. Furthermore, the addition of Mn inhibited the aggregation of TiO_2 nanoparticles which also resulted in a larger specific surface area.

The X-ray diffraction (XRD) patterns of the catalysts are shown in Fig. 2. The anatase phase (2θ=25.3°, 37.7°, 48.1°, 53.9°, 56.1°, 62.8°, 69.1°, 70.3°, 75.3°, 82.9°) and rutile phase (2θ=27.5°, 36.1°, 41.3°, 44°, 54.4°, 64°) were observed in pure TiO_2 crystalline, and the anatase phase accounts for more than 73%. The anatase phase was found to be the only crystalline phase in Mn-doped TiO_2. The diffraction peaks of the anatase phase of TiO_2 in Mn(x)-TiO_2 became broader and weaker with the increasing of the Mn loading value, which indicated that the anatase phase of TiO_2 with the smaller crystallite size [16,17]. The crystallite size of catalysts was determined using the Scherrer equation [18] and the crystallite sizes of TiO_2 and Mn(x)-TiO_2 (x=1, 3, 5, 10, 15) were 19.3, 17, 14.6, 13.3, 12 nm, and 11.8 nm, respectively. This result suggested that

Table 1. Experimental conditions

Sets	Catalysts	O_2 (%)	SO_2 (ppmv)	NO (ppmv)	H_2O (%)	N_2 (%)
1	TiO_2, Mn(x)-TiO_2 x=1, 3, 5, 10, 15	6	0	0	0	Balance
2	Mn(10)-TiO_2	0, 3, 6	0	0	0	Balance
3	Mn(10)-TiO_2	0	0	42, 250, 500	0	Balance
4	Mn(10)-TiO_2	0	42, 300, 600	0, 500	0	Balance
5	Mn(10)-TiO_2	6	600	500	0, 2, 8	Balance

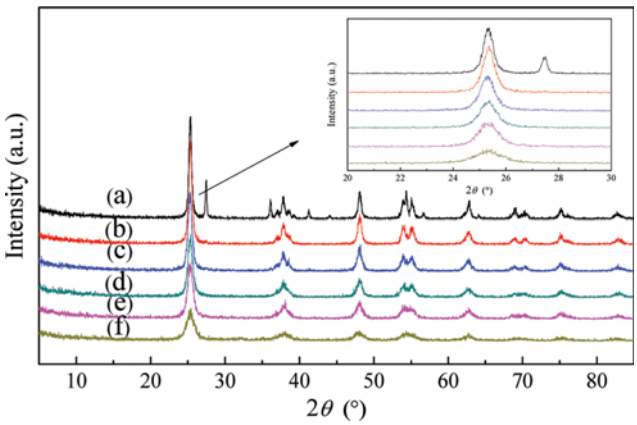

Fig. 2. XRD patterns of the Mn(x)-TiO_2 samples with different x values. (a) x=0; (b) x=1; (c) x=3; (d) x=5; (e) x=10; (f) x=15.

introduction of Mn inhibited the grain growth of TiO_2 crystallite. The diffraction peaks corresponding to MnO_x were not observed in all XRD patterns. However, the peaks corresponding to MnO_x were detected in the XPS spectra, which indicated that the Mn species were highly dispersed on the surface of catalysts and existed as the amorphous phase [19,20].

The mechanism and the reaction pathways for Hg^0 catalytic oxidation and adsorption have not been well understood yet. To determine the changes of the chemical states of the main elements on catalysts and the speciation of the adsorbed mercury, XPS techniques were used to analyze the samples of the fresh and spent catalyst.

The XPS spectra of Ti 2*p*, O 1*s*, Mn $2p_{3/2}$ and Hg 4*f* on the Mn(10)-TiO_2 with or without adsorbed mercury were scanned and the results are shown in Fig. 3. For the fresh Mn(10)-TiO_2, two main peaks due to Ti $2p_{3/2}$ and Ti $2p_{1/2}$ were observed at 458.6 eV and 464.7 eV in Fig. 3(a), which indicated the presence of typical Ti^{4+}. There was no significant change for the binding energy and intensity peak of Ti 2*p* in the spent Mn(10)-TiO_2, and the binding energy of Ti $2p_{3/2}$ and Ti $2p_{1/2}$ was 458.3 eV and 464.5 eV, respectively. It indicated that Ti^{4+} in Mn(10)-TiO_2 was the inactive substance in the process of Hg^0 oxidation. Various oxygen species on the surface of fresh and spent Mn(10)-TiO_2 are shown in Fig. 3(b). The peaks corresponding to lattice oxygen (O^{2-}) were observed at 529.6 eV on fresh Mn(10)-TiO_2 and at 529.4 eV on spent Mn(10)-TiO_2, respectively. The peaks at 531.2 eV and 530.5 eV corresponded to the weakly adsorbed oxygen. The peak at 532.2 eV on the spent catalyst represents the hydroxyl (-OH) and H_2O bonded oxygen. Compared with the spectra of the fresh catalyst, O 1*s* peak of the spent catalyst became broader and weaker, which could be attributed to the formation of HgO and the adsorption of H_2O molecules [14]. Fig. 3(c) shows the spectra of Mn $2p_{3/2}$. The binding energies of two peaks were observed at 641.7 eV and 642.9 eV on fresh Mn(10)-TiO_2, which corresponded to Mn^{3+} and Mn^{4+}, respectively. No obvious peak change was found in the spent Mn(10)-TiO_2 and the peaks corresponding to Mn^{3+} and Mn^{4+} were located at 641.7 eV and 643.4 eV. However, the intensity of Mn $2p_{3/2}$ peaks changed significantly.

The ratio of the spectra area with respect to Mn^{3+} and Mn^{4+} was about 0.5 for the fresh catalyst, but the ratio increased to 1.2 for the spent catalyst. The results indicated that Mn^{4+} was converted partially to Mn^{3+} during the absorption process and the MnO_x was involved in the reaction with Hg^0 oxidation.

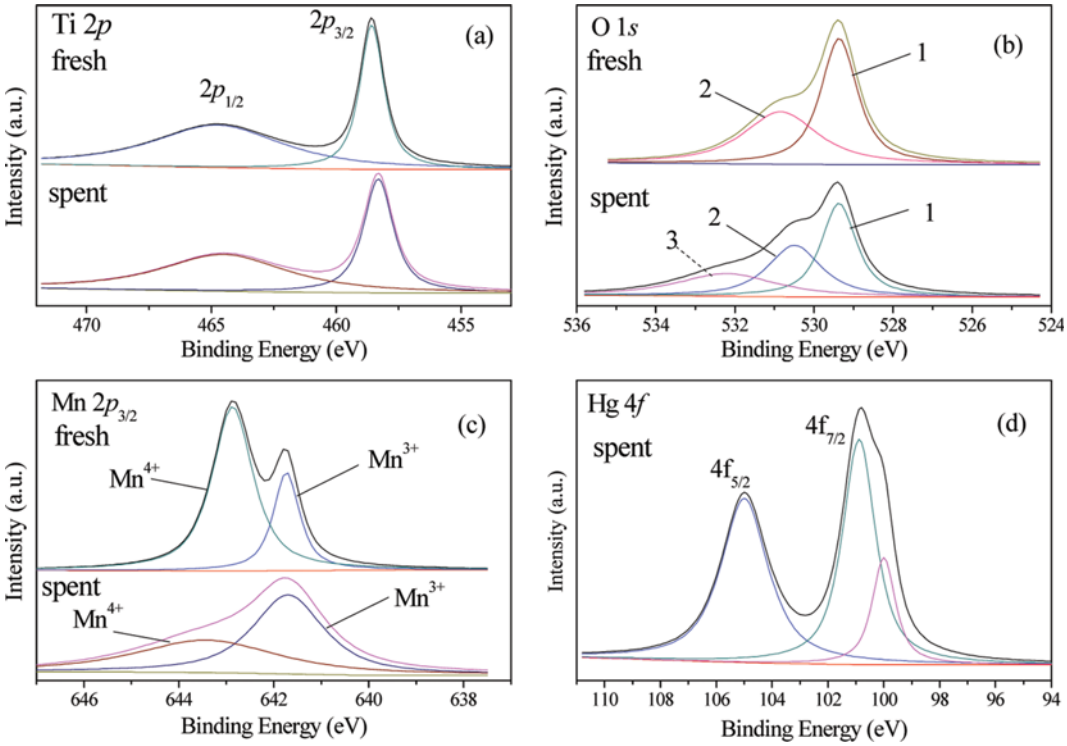

Fig. 3. XPS spectra of Mn(10)-TiO_2. (a)-(c) Ti 2*p*, O 1*s* and Mn $2p_{3/2}$ spectra of fresh and spent Mn(10)-TiO_2; (d) Hg 4*f* spectra of spent Mn(10)-TiO_2.

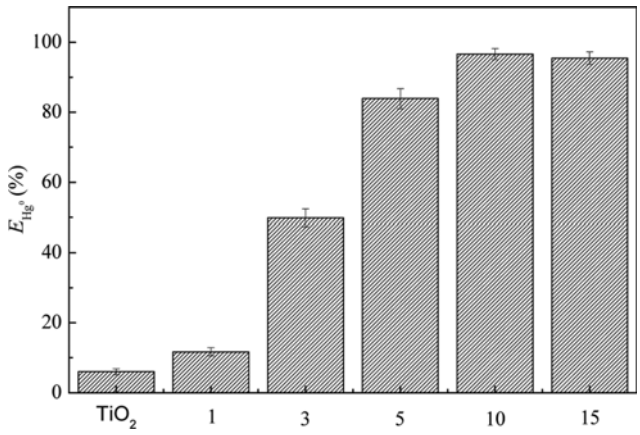

Fig. 4. Performance of TiO_2 and Mn(x)-TiO_2 on Hg^0 removal. x=1, 3, 5, 10, 15 (N_2/6%O_2, 120 °C; adsorption time, 4 h; gas flow rate, 2.2 L·min^{-1}; catalyst mass, 0.5 g).

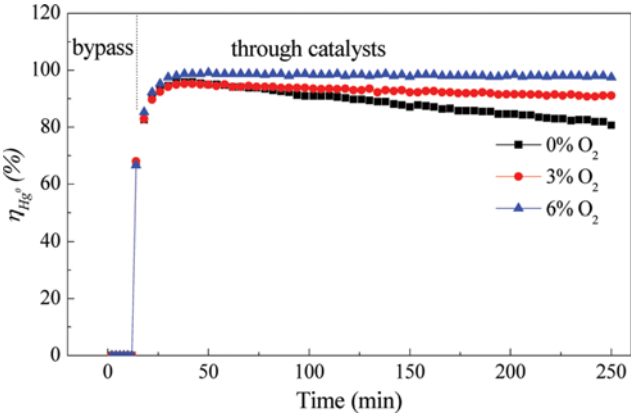

Fig. 5. Effect of O_2 on the Hg^0 removal over Mn(10)-TiO_2 (120 °C; gas flow rate, 2.2 L·min^{-1}; Mn(10)-TiO_2; catalyst mass, 0.5 g).

To determine the speciation of mercury on the surface of the spent Mn(10)-TiO_2 catalyst, XPS analysis was performed and the spectra of Hg 4f in the range from 94 eV to 110 eV are shown in Fig. 3(d). The spectra of Hg 4f7/2 can be divided into two peaks at 100.9 eV and 100 eV, respectively. The peak at 100.9 eV was determined to be the response from the oxidized mercury, while the peak at 100 eV was related to the weakly adsorbed Hg^0. The results indicated that Hg^0 was adsorbed and then partially oxidized by the chemisorbed oxygen on the surface of catalyst. The appearance of Hg^0 on the spent catalyst surface was attributed to the adsorption site and the strong affinity between oxidized mercury and Hg^0 [21].

2. Performance of Mn(x)-TiO_2

The effects of the Mn content on the Hg^0 removal efficiency are shown in Fig. 4. E^0_{Hg} was only 6% for the pure TiO_2, which was similar to the results of Kamata et al. [22]. The removal efficiency of Hg^0 increased from 6% to 97% with the increasing of the Mn/Ti molar ratio from 0 to 15. The positive effect of Mn loading content on the Hg^0 removal efficiency was attributed to the improvement of the porous structure property of catalyst, as indicated in Table 2. The better porous property promoted the physical adsorption process, and thus increased the probability of the contact between Hg^0 with the active site on the surface of Mn-TiO_2. Moreover, the XRD results indicated that the addition of Mn enhanced TiO_2 crystalline conversion from the rutile phase to anatase phase. The catalytic activity of TiO_2 was also enhanced. After Mn^{4+} entered the TiO_2 lattice, some parts of Ti^{4+} would be substituted, which caused lattice distortion. More chemisorbed oxygen functional group on Mn-TiO_2 surface was observed by XRD results, which enhanced the chemical adsorption and oxidation process of the Hg^0.

3. Effects of the Main Components in Flue Gas

3-1. Effect of O_2

The positive effect of O_2 on the Hg^0 removal over the Mn(10)-TiO_2 catalyst is shown in Fig. 5. A mass balance calculation was also performed to ensure the accuracy and reliability of the experiments and the results are shown in Table 3. Generally, the Mars–Maessen mechanism was proposed to understand the reactions on the surface of Mn(x)-TiO_2 catalyst [23,24]. The gaseous Hg^0 was adsorbed on the surface of Mn(x)-TiO_2 to form Hg^0(ad) by physical adsorption and then was oxidized to HgO by the surface oxygen O* [25,26] which included the lattice oxygen in manganese dioxide and chemisorbed oxygen. Meanwhile, Mn^{4+} was also reduced to Mn^{3+}. The uptake of the lattice oxygen by mercury over the catalyst was compensated by activating the gaseous oxygen from the gas.

$$Hg^0(g) \rightarrow Hg^0(ad) \quad (7)$$

$$MnO_2 \rightarrow Mn_2O_3 + O^* \quad (8)$$

$$Hg^0(ad) + O^* \rightarrow HgO \quad (9)$$

$$Mn_2O_3 + 1/2O_2 \rightarrow 2MnO_2 \quad (10)$$

Where O* refers the lattice oxygen in manganese dioxide and chemisorbed oxygen on the surface of Mn(10)-TiO_2.

3-2. Effect of NO

In the literature, the effect of NO on Hg^0 oxidation over metal oxide catalysts in flue gas is not conclusive. Both promotional and inhibitory effects have been reported [27,28]. In our study, a slight

Table 3. The mercury speciation and mass balance calculation for test condition of set 2 (adsorption time, 4 h, gas flow rate, 2.2 L·min^{-1}, catalyst mass, 0.5 g)

Experimental condition	Inlet (μg/m^3)			Adsorbed mercury on catalysts (μg/g)	Outlet (μg/m^3)			Mass balance (%)
	Hg^0	Hg^{2+}	Hg^T		Hg^0	Hg^{2+}	Hg^T	
Mn(10)-TiO_2, without O_2	57.3	0.3	57.6	52.7	6.6	0.1	6.7	98.3
Mn(10)-TiO_2, with 3% O_2	58.2	2.3	60.5	56.7	4.5	0.1	4.7	96.5
Mn(10)-TiO_2, with 6%O_2	56.9	3.0	59.9	55.1	1.5	0.2	1.6	94.7

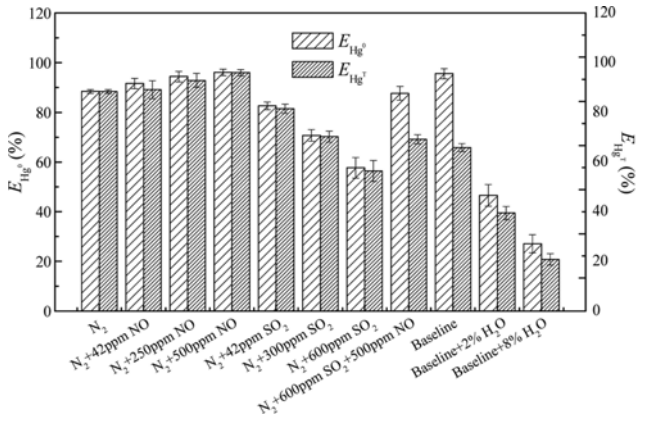

Fig. 6. Effects of NO, SO_2 and H_2O on mercury removal (Baseline: N_2+6%O_2+600 ppm SO_2+500 ppm NO; 120 °C; adsorption time, 4 h; gas flow rate, 2.2 L·min^{-1}; Mn(10)-TiO_2; catalyst mass, 0.5 g).

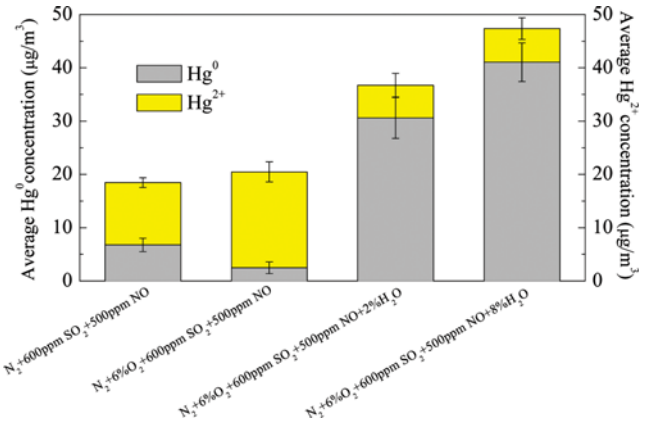

Fig. 7. Mercury speciation distribution in effluent gas under complex flue gas atmosphere (120 °C; time, 4 h; gas flow rate, 2.2 L·min^{-1}; Mn(10)-TiO_2; catalyst mass, 0.5 g).

promotional effect of NO on Hg^0 oxidation and capture over the Mn(x)-TiO_2 catalyst was observed. As illustrated in Fig. 6, E^0_{Hg} and E^T_{Hg} increased from 91.6% and 89.2% to 96.1% and 96%, respectively, with the increasing of NO from 42 to 500 ppmv. The possible reason can be attributed to the following pathway: Both Hg^0 and NO are adsorbed on the surface of catalyst, and the adsorbed NO can be oxidized on the surface of metal oxide catalysts by MnO_x to form abundant active species like NO_2 which is likely responsible for Hg^0 oxidation [29,30]. However, the promotional effect was not significant because the adsorption of NO on metal based catalysts was weak [31].

$$2MnO_2+NO \rightarrow Mn_2O_3+NO_2 \quad (11)$$

$$NO_2+Hg^0(ad) \rightarrow NO+HgO \quad (12)$$

3-3. Effect of SO_2

In the literature, the effect of SO_2 on Hg^0 oxidation over metal oxide catalysts in flue gas is not conclusive. Promotional [32], inhibitive [33], have all been reported. However, in our work, the effect of SO_2 on Hg^0 oxidation over the Mn(x)-TiO_2 catalyst was found to be inhibitory. As shown in Fig. 6, the E^0_{Hg} and E^T_{Hg} decrease from 82.6% and 81.5% to 57.7% and 56.4%, respectively, with the addition of SO_2 increasing from 42 ppm to 600 ppm. This indicates SO_2 inhibited Hg^0 oxidation over the Mn(x)-TiO_2 catalyst. This result could be attributed to the competitive adsorption for the active sites between SO_2 and Hg^0 on the surface of catalysts [34]. The adsorbed SO_2 could react with the manganese oxide to form manganese sulfate. Moreover, these adsorbed SO_2 could also react with surface oxygen to form SO_3 [35,36], which consume the limited surface oxygen. On the other hand, the new generated manganese sulfate and SO_3 would occupy the active sites [35], leading to a further decreasing of Hg^0 adsorption.

3-4. Effect of H_2O

Moisture is one of the main components of coal-fired flue gases and often leads to lower catalyst performance. H_2O has been reported to inhibit Hg^0 oxidation and removal over metal oxide catalysts due to competitive adsorption [32]. A significant inhibitory effect of H_2O on Hg^0 oxidation was observed over the Mn-TiO_2 catalyst in our experiments; the result is illustrated in Fig. 6. Under the condition of Set 5 without H_2O in simulated flue gas, E^0_{Hg} and E^T_{Hg} were 95.6% and 65.8%, respectively. When 2% H_2O was introduced, E^0_{Hg} and E^T_{Hg} decreased to 45.6% and 39.5%. As the water vapor concentration further increased from 2% to 8% in the flue gas system, E^0_{Hg} and E^T_{Hg} decreased to 27.1% and 20.8%. These behaviors are consistent with the other literature [39]. The extent of inhibition on Hg removal is proportional to the concentration of water vapor. The inhibitory effect could be attributed to competitive adsorption between Hg^0 and H_2O on the catalysts surface. H_2O would occupy the active sites and inhibit the adsorption of Hg^0 [39]. H_2O could also react with SO_3 to form H_2SO_4, which covered the active sites [29].

4. Mercury Speciation under a Complex Flue Gas Atmosphere

Mercury speciation in the effluent gas under complex flue gas atmosphere was also investigated and the results given in Fig. 7. A higher proportion of Hg^{2+} content in effluent gas was found under N_2+O_2+SO_2+NO condition. This fact was attributed to the formation of the volatile mercuric nitrate $Hg(NO_3)_2$ on the surface of Mn-TiO_2 catalyst. Olson et al. [40] also studied the Hg speciation in the effluent gas under the NO_x/SO_2 atmosphere used GC-MS technique, and the results showed that the Hg^{2+} formed over MnO_2 in the flue gas was mainly mercuric nitrate $Hg(NO_3)_2$. Due to the (79 °C) of $Hg(NO_3)_2$ [30], a part of $Hg(NO_3)_2$ would volatilize into the flue gas at the experimental temperature (120 °C).

5. Thermal Stability of Mercury Captured on Mn-TiO_2

Thermal stability of mercury captured by a sorbent/catalyst is an important property because it relates to release of Hg to the gas phase. Fig. 8 shows the reemission behavior of Hg captured on Mn(10)-TiO_2 in temperature programmed desorption (TPD) experiments in N_2. Four different spent Mn(10)-TiO_2 catalysts, which were used in the adsorption test under the pure N_2, N_2+6%O_2, N_2+500 ppmNO and N_2+600 ppmSO_2 atmosphere, were tested in the TPD experiment. It was observed that the Hg release occurs in a temperature range of 100 to 600 °C. The initial Hg release temperature, around 150 °C, is a crucial parameter to determine the optimum temperature (around 120 °C) for Hg^0 capture in our study.

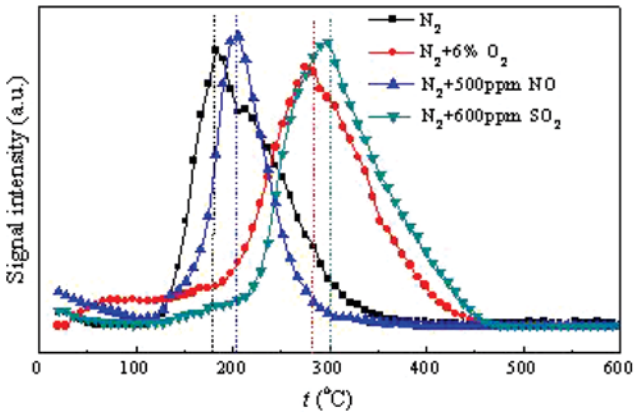

Fig. 8. TPD-Hg profiles of the spent Mn(10)-TiO_2.

Four TPD-Hg profiles show different Hg desorption peaks at different temperatures, which may be attributed to the different occurrence of mercury on the surface of Mn(10)-TiO_2. The two lower desorption temperatures peaks were related to the high volatile property of elemental mercury and $Hg(NO_3)_2$ adsorbed on catalyst under pure N_2 and N_2+500 ppmNO atmosphere. But the two higher temperature peaks (around at 290 °C) may be attributed to the different reduction temperatures of HgO and $HgSO_4$ which were generated under N_2+6%O_2 and N_2+500 ppmSO_2 atmosphere [41]. Note that more than 95% Hg captured on catalyst is released during the TPD experiments.

CONCLUSIONS

Mn(*x*)-TiO_2 prepared by a sol-gel method exhibited high activity for the oxidation of Hg^0 at 120 °C. XPS results demonstrated that Mn^{4+} converted into Mn^{3+} in Hg^0 oxidation process and Hg^0 was oxidized into HgO. Since O_2 could replenish the surface oxygen, it had a promotional effect on Hg^0 oxidation. Due to the consumption of surface oxygen and competition for the active sites, the presence of SO_2 in flue gas was not beneficial for Hg^0 oxidation. The formation of NO_2 exhibited a positive influence on Hg^0 oxidation while introducing NO in flue gas. H_2O showed an inhibitory effect on Hg^0 removal and capture. The inhibitory effect can be explained by its competitive occupancy of adsorption sites and displacement of adsorbed Hg^0 on the surface of catalyst. The simultaneous presence of NO and SO_2 resulted in a significant increase of Hg^{2+} concentration in the outlet flue gas, which may be attributed to the formation of $Hg(NO_3)_2$.

ACKNOWLEDGEMENTS

This work was financially supported by National Natural Science Foundation of China (No. 51506099, 50976049), the Natural Science Foundation of Jiangsu (BK20130906), and the Natural Science Foundation for Colleges of Jiangsu Province (13KJB610011).

REFERENCES

1. Q. Wan, L. Duan, K. B. He and J. H. Li, *Chem. Eng. J.*, **170**, 512 (2011).
2. Y. Wu, S. X. Wang, D. G. Streets, J. M. Hao, M. Chan and J. K. Jiang, *Environ. Sci. Technol.*, **40**, 5312 (2006).
3. J. B. Milford and A. Pienciak, *Environ. Sci. Technol.*, **43**, 2669 (2009).
4. U.S. Environmental Protection Agency. Air Toxics Standards for Utilities, http://www.epa.gov/airquality/powerplanttoxics/actions.html (Accessed on June 2012).
5. Z. Q. Tan, L. S. Sun, J. Xiang, H. C. Zeng, Z. H. Liu, S. Hu and J. R. Qiu, *Carbon*, **50**, 362 (2012).
6. T. M. Tang, J. Xu, R. J. Lu, J. J. Wo and X. H. Xu, *Fuel*, **89**, 3613 (2010).
7. H. Yang and W. P. Pan, *J. Environ. Sci.*, **19**(2), 181 (2007).
8. J. E. Granite, W. H. Pennline and A. R. Hargis, *Ind. Eng. Chem. Res.*, **39**, 1020 (2000).
9. J. F. Li, N. Q. Yan, Z. Qu, S. H. Qiao, S. J. Yang, Y. F. Guo, P. Liu and J. P. Jia, *Environ. Sci. Technol.*, **44**, 426 (2009).
10. J. He, G. K. Reddy, S. W. Thiel, P. G. Smirniotis and N. G. Pinto, *Energy Fuels*, **27**, 4832 (2013).
11. S. J. Yang, N. Q. Yan, Y. F. Guo, D. Q. Wu, H. P. He, Z. Qu, J. F. Li, Q. Zhou and J. P. Jia, *Environ. Sci. Technol.*, **45**, 1540 (2011).
12. J. K. Xie, N. Q. Yan, S. J. Yang, Z. Qu, W. M. Chen, W. Q. Zhang, K. H. Li, P. Liu and J. J. S. Jia, *Res. Chem. Intermed.*, **38**, 2511 (2012).
13. L. Ji, P. M. Sreekanth, P. G. Smirniotis, S. W. Thiel and N. G. Pinto, *Energy Fuels*, **22**, 2299 (2008).
14. E. J. Granite, H. W. Pennline and R. A. Hargis, *Ind. Eng. Chem. Res.*, **39**, 1020 (2000).
15. Y. Li, P. Murphy and C. Y. Wu, *Fuel Process. Technol.*, **89**, 567 (2008).
16. H. Liu, X. Q. Yu and H. M. Yang, *Chem. Eng. J.*, **243**, 465 (2014).
17. C. Gionco, M. C. Paganini, S. Agnoli, A. E. Reeder and E. J. Giamello, *Mater. Chem. A.*, **1**, 10918 (2013).
18. J. G. Yu and J. R. Ran, *Energy Environ. Sci.*, **4**, 1364 (2011).
19. S. S. Kim and S. C. Hong, *J. Air Waste Manage.*, **62**, 362 (2012).
20. E. Park, H. Le, S. Chin, J. Kim, G. N. Bae and J. Jurng, *J. Porous. Mat.*, **19**, 877 (2012).
21. E. Pitoniak, C. Y. Wu, D. W. Mazyck, K. W. Powers and W. Sigmund, *Environ. Sci. Technol.*, **39**, 1269 (2005).
22. H. Kamata, S. Ueno, T. Naito, A. Yamaguchi and S. Ito, *Catal. Commun.*, **9**, 2441 (2008).
23. S. H. Qiao, J. Chen, J. F. Li, Z. Qu, N. Q. Yan and J. P. Jia, *Ind. Eng. Chem. Res.*, **48**, 3317 (2009).
24. F. H. Kong, J. R. Qiu, H. Liu, R. Zhao and Z. H. Ai, *J. Environ. Sci.*, **23**, 699 (2011).
25. H. L. Li, C. Y. Wu, Y. Li, L. Q. Li, Y. C. Zhao and J. Y. Zhang, *Chem. Eng. J.*, **219**, 319 (2013).
26. J. He, G. K. Reddy, S. W. Thiel, P. G. Smirniotis and N. G. Pinto, *J. Phys. Chem. C.*, **115**, 24300 (2011).
27. G. A. Norton, H. Q. Yang, R. C. Brown, D. L. Laudal, G. E. Dunham and J. Erjavec, *Fuel*, **82**, 107 (2003).
28. H. L. Li, C. Y. Wu, Y. Li, L. Q. Li, Y. C. Zhao and J. Y. Zhang, *J. Hazard. Mater.*, **243**, 117 (2012).
29. X. Y. Wen, C. T. Li, X. P. Fan, H. L. Gao, W. Zhang, L. Zhang, G. M. Zeng and Y. P. Zhao, *Energy Fuels*, **25**, 2939 (2011).
30. Y. Li, P. D. Murphy, C. Y. Wu, K. W. Powers and J. C. J. Bonzongo, *Environ. Sci. Technol.*, **42**, 5304 (2008).
31. H. L. Li, Y. Li, C. Y. Wu and J. Y. Zhang, *Chem. Eng. J.*, **169**, 186 (2011).

32. H. L. Li, Y. Li, C. Y. Wu and J. Y. Zhang, *Chem. Eng. J.*, **169**, 186 (2011).
33. J. F. Li, N. Q. Yan, Z. Qu, S. H. Qiao, S. J. Yang, Y. F. Guo, P. Liu and J. P. Jia, *Environ. Sci. Technol.*, **44**, 426 (2010).
34. C. X. Hu, J. S. Zhou, Z. Y. Luo and K. F. Cen, *Energy Fuels*, **25**, 154 (2010).
35. Z. B. Wu, R. B. Jin, H. Q. Wang and Y. Liu, *Catal. Commun.*, **10**, 935 (2009).
36. M. H. Kim, S. W. Ham and J. B. Lee, *Appl. Catal., B.*, **99**, 272 (2010).
37. W. Q. Xu, H. He and Y. B. Yu, *J. Phys. Chem. C.*, **113**, 4426 (2009).
38. H. L. Li, C. Y. Wu, Y. Li and J. Y. Zhang, *Environ. Sci. Technol.*, **45**, 7394 (2011).
39. J. S. Zhou, W. H. Hou, P. Qi, X. Gao, Z. Y. Luo and K. F. Cen, *Environ. Sci. Technol.*, **47**, 10056 (2013).
40. E. S. Olson, J. S. Thompson and J. H. Pavlish, *Prepr. ACS Div. Fuel Chem.*, **45**, 560 (2000).
41. S. Guo, J. Yang, Z. Liu and Y. Xiao, *Korean J. Chem. Eng.*, **26**, 560 (2009).